

## Article

# On the Impact of the Intermetallic Fe<sub>2</sub>Nb Laves Phase on the Mechanical Properties of Fe-6 Al-1.25 Nb-X W/ Mo Fully Ferritic Light-Weight Steels

Robin Emmrich \*  and Ulrich Krupp

Steel Institute of RWTH, Aachen University (IEHK), Intzestr. 1, 52072 Aachen, Germany; krupp@iehk.rwth-aachen.de

\* Correspondence: robin.emmrich@iehk.rwth-aachen.de; Tel.: +49-241-80-95824

**Abstract:** The present study aims at the development of precipitation hardening fully ferritic steels with increased aluminum and niobium content for application at elevated temperatures. The first and second material batch were alloyed with tungsten or molybdenum, respectively. To analyze the influence of these elements on the thermally induced precipitation of the intermetallic Fe<sub>2</sub>Nb Laves phase and thus on the mechanical properties, aging treatments with varying temperature and holding time are performed followed by X-ray diffraction (XRD) analysis and scanning electron microscopy (SEM) including elemental contrast based particle analysis as well as hardness measurements and tensile tests at room temperature and at 500 °C. The incorporation of molybdenum into the Laves phase sets in at an earlier stage of aging than the incorporation of tungsten, which leads to faster growth and coarsening of the Laves phase in the molybdenum-alloyed steel. Nevertheless, both concepts show a fast and massive increase in hardness (280 HV10) due to precipitation of Laves phase during aging at 650 °C. After 4 h aging, the yield strength increase at room temperature is 100 MPa, which stays stable at operation temperatures up to 500 °C.

**Keywords:** laves phase; Fe<sub>2</sub>Nb; Fe-Al; tungsten; molybdenum; precipitation; aging; ferrite; SEM; XRD; light weight



**Citation:** Emmrich, R.; Krupp, U. On the Impact of the Intermetallic Fe<sub>2</sub>Nb Laves Phase on the Mechanical Properties of Fe-6 Al-1.25 Nb-X W/ Mo Fully Ferritic Light-Weight Steels. *Metals* **2021**, *11*, 1693. <https://doi.org/10.3390/met11111693>

Academic Editors: Mohamed Soliman and Dong-Woo Suh

Received: 3 September 2021  
Accepted: 19 October 2021  
Published: 24 October 2021

**Publisher's Note:** MDPI stays neutral with regard to jurisdictional claims in published maps and institutional affiliations.



**Copyright:** © 2021 by the authors. Licensee MDPI, Basel, Switzerland. This article is an open access article distributed under the terms and conditions of the Creative Commons Attribution (CC BY) license (<https://creativecommons.org/licenses/by/4.0/>).

## 1. Introduction

For automotive power train application, nowadays, steels such as 42CrMo4 and 38MnVS6 are widely used for medium-temperature service up to 350 °C [1–3]. The disadvantage of these steels is their low resistance to scaling at temperatures above this limit [3–5]. Therefore, it is not possible to increase the process temperature and thus the efficiency level of modern internal combustion engines and the overall power train, respectively. In addition, their high density in comparison to other materials used for rotating parts (Al alloys, carbon fiber reinforced plastics) is a drawback in terms of fuel efficiency and CO<sub>2</sub> emission [1,6].

For high-temperature service up to 900 °C, steels with high Cr-contents of about 18 wt. %, such as X2CrTiNb18, are used [7,8], since they have a better resistance to scaling [9]. Furthermore, alloying with this amount of Cr leads to fully ferritic microstructure without phase transformation during cooling, which is advantageous for distortion-free cooling after forging. However, the high Cr-content makes this steel cost intensive and thus uneconomical for applications at medium temperatures. Reducing the Cr-content to a range of 9 to 12 wt. %, which is still sufficient for good resistance to scaling at temperatures below 620 °C, leads to a ferritic-martensitic microstructure [10,11]. Thus, the benefit of distortion-free cooling is lost.

In order to be able to combine oxidation resistance [12], fully ferritic microstructure [13] and lower material density [14], Al was chosen as the main alloying element instead of Cr in the investigated steel alloys. Unfortunately, Fe-Al alloys tend to have a low yield

strength [15]. However, it has been shown in previous works [15,16] that the yield strength can be effectively increased even at high temperatures by alloying with Nb, which leads to the precipitation of the intermetallic Laves phase. The studies conducted so far in this field [15–19] focus on the precipitates occurring in Fe-Al-Nb alloys in dependency on the aging temperature. The influence of technical aging processes on the resulting mechanical properties has not yet been considered.

The Laves phase is the most frequently occurring phase among intermetallic compounds. It offers an enormous potential to increase high-temperature strength and creep resistance through precipitation hardening, as it is thermally very stable and has only a small tendency to coarsen during service at elevated temperatures [20–23]. Alloying heat-resistant 18 wt. % Cr steels with Nb, W, and/or Mo leads to the formation of the hexagonal C14 Laves phase [24,25]. This phase has a B<sub>2</sub>A structure, where the B atoms are Fe and the A atoms are Nb, W, or Mo [26,27]. In technical applications, however, it has often been demonstrated that several different A atoms (Nb, W, Mo) can be incorporated into the Laves phase at the same time. On the side of the B atoms, Fe can be partly replaced by Si and, in Cr-alloyed steels, also by Cr. [10,20–23,28–30]

The present study aims to assess the potential of the intermetallic Laves phase (Fe<sub>2</sub>Nb) on the mechanical properties of newly developed aluminium-alloyed light-weight forging steels for automotive powertrain applications. The further development of a Fe-6 wt. % Al-1.25 wt. % Nb steel by alloying with 1.25 wt. % W and 0.75 wt. % Mo, respectively, is carried out in this work. By the novel combination of Nb and W or rather Nb and Mo in Fe-Al alloys, the influence of W and Mo on the coarsening behaviour of the Fe<sub>2</sub>Nb Laves phase and thus on the mechanical properties is studied. Heat treatments with varying temperature and holding time are performed to investigate the influence of technical aging processes on the precipitation hardening of Fe-Al-Nb-W/Mo alloys, which has even not been considered so far for Fe-Al-Nb alloys. After aging, X-ray diffraction analysis (XRD) as well as an intensive particle analysis using scanning electron microscopy (SEM) images are carried out. The mechanical properties are determined by means of tensile tests at room temperature and at 500 °C and hardness measurements.

## 2. Materials and Methods

Two 75 kg laboratory melts were produced in a vacuum induction furnace and cast to ingots with a size of 140 mm × 140 mm × 500 mm. After solidification, the ingots were homogenized in a resistance-heated furnace at 1200 °C for 2 h and subsequently forged to a cross-section of 60 mm × 60 mm. The forged bars were air-cooled to room temperature. Special feature of the laboratory melts is the high Al content of 6 wt. %, which serves to protect against oxidation and ensures cooling without phase transformations. Apart from that, the two laboratory melts differ only in W and Mo content. Alloy 1 (W-concept) was alloyed with 1.25 wt. % W, while for alloy 2 (Mo-concept), W was stoichiometrically replaced by Mo (resulting in 0.75 wt. % Mo). In addition to W and Mo, both steels are alloyed with 1.30 wt. % Nb, which is an effective Laves phase former. The C content was chosen as low as possible on large-scale industrial level to suppress carbide precipitation and to avoid aging processes. The chemical compositions of both alloys are displayed in Table 1. The selection of the alloying concepts was based on THERMOCALC simulations using TCFE9 database.

**Table 1.** Chemical composition of the two steels analyzed with spark spectral analysis.

Alloy		C *	Si	Mn	S *	Al	N	W	Mo	Nb	Fe
W-concept	wt. %	0.021	0.50	0.25	0.002	5.91	0.007	1.23	–	1.34	bal.
	at. %	0.093	0.94	0.24	0.003	11.59	0.026	0.35	–	0.76	bal.
Mo-concept	wt. %	0.029	0.50	0.27	0.013	5.91	0.004	–	0.75	1.29	bal.
	at. %	0.127	0.94	0.26	0.021	11.53	0.015	–	0.41	0.76	bal.

\* C, S determined with Leco-combustion analysis

To tailor the precipitation of Laves phase, heat treatments were performed in a BÄHR 805 A/D dilatometer under argon atmosphere on samples with a size of 7.0 mm × 4.0 mm × 1.4 mm. During forging and air-cooling, strain-induced precipitation of inadvertent large Laves phase particles took place. To investigate the influence of aging on the precipitation of the Laves phase, it is mandatory to conduct solution annealing (1250 °C, 1h) to dissolve this phase followed by quenching to room temperature (cooling rate 150 K/s). Quenching was followed directly by an aging treatment for 0.5–192 h to thermally induce precipitation of the Laves phase. Based on thermodynamic simulations, temperatures of 550, 650, and 750 °C were selected for aging. The applied process chain is displayed in Figure 1.

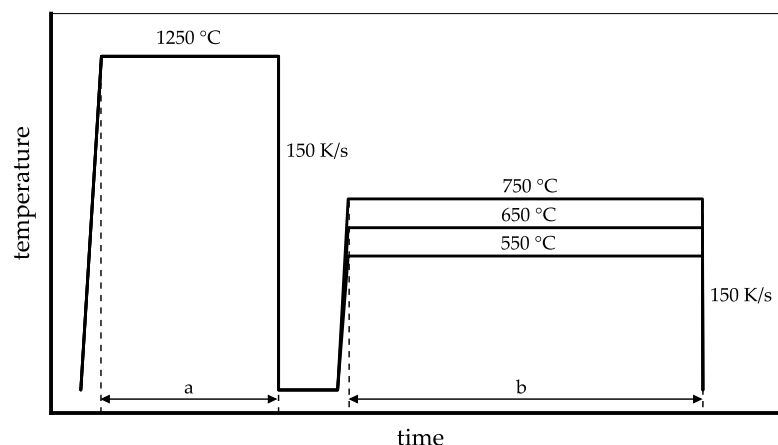


**Figure 1.** Temperature and holding times ( $a = 1$  h;  $b = 0.5, 1, 2, 4, 6, 8, 12, 24, 48, 96,$  and  $192$  h) for the applied heat treatments.

Afterwards, heat-treated samples were ground with SiC paper to P2500 and then polished in three stages with diamond suspension (6, 3, 1  $\mu\text{m}$ ) with a SAPHIR 550 semi automatic grinding and polishing machine from QATM. The final polishing was carried out on a SAPHIR VIBRO vibration polishing machine from QATM with ultrafine polishing suspension ( $\text{Al}_2\text{O}_3$ , grain size 0.06  $\mu\text{m}$ ).

The scanning electron microscopic (SEM) examination was carried out by means of a ZEISS SIGMA field emission gun SEM. Backscattered electron (BSE) images were taken with an accelerating voltage of 10 kV and a working distance of 8.5 mm to obtain the optimum contrast of the precipitates. To ensure consistent results, brightness and contrast were kept equal for all images. Secondary electron (SE) images with the same accelerating voltage and working distance were taken for overview. The chemical composition of matrix and precipitates was determined by means of energy dispersive X-ray spectroscopy (EDS) using an OXFORD INSTRUMENTS X-MAX<sup>N</sup> detector operating with AZTEC<sup>®</sup> 5.0 software.

Furthermore, X-ray diffraction analysis was performed to identify the phases using an EMPYREAN X-ray diffractometer from PANALYTICAL with Co  $K\alpha$  radiation ( $\lambda = 1.7889$  Å). For data logging PANALYTICAL's HIGHSCORE PLUS software was used. The measurements were performed in a  $2\theta$  range of 30–110° with a stepsize of 0.01°. Diffraction analysis was performed with MAUD analysis software using ferrite [31],  $\text{Fe}_2\text{Nb}$  [32], AlN [33], NbC [34],  $\text{Fe}_3\text{Al}$  [35], and FeAl [36] database.

Determination of Laves phase particle size was performed by analyzing a minimum of ten grains per sample using a magnification of 10,000 $\times$ . The images were analyzed using IMAGEJ image analysis software. Particular attention was paid to the ferret diameter and the area of the particles. The area was then used to calculate the equivalent circle diameter (ECD), which is used to classify the particle sizes. To avoid falsifications by background noise, only particles with an area of more than 10 pixels were considered in the evaluation.

Additionally, Vickers hardness was determined according to DIN EN ISO 6507-1 and stress–strain curves were determined at room temperature and at 500 °C in quasistatic tensile tests on a electromechanical tensile testing machine (ZWICKROELL Z100) using round

tensile samples of B6 × 30 geometry. Solution annealing (1 h at 1250 °C) and aging (4 h at 650 °C) of the tensile samples took place in a resistance-heated furnace (THERMCONCEPT KM15\13 equipped with a RHODE TC 504 control unit). To protect against oxidation during solution annealing and aging the samples were wrapped in oxidation protection foil. After both heat treatments, water quenching was applied.

### 3. Results and Discussion

#### 3.1. Microstructure Analysis and Thermodynamic Assessment

The results of equilibrium thermodynamic simulation for both alloys are given in Figure 2. In both steels, AlN forms during solidification, while NbC and MnS precipitate shortly before complete solidification. Due to the high Al content and the addition of Si, a fully ferritic microstructure is predicted for cooling from liquids to room temperature. This influence of Al on the microstructure was also reported by Palm [13].

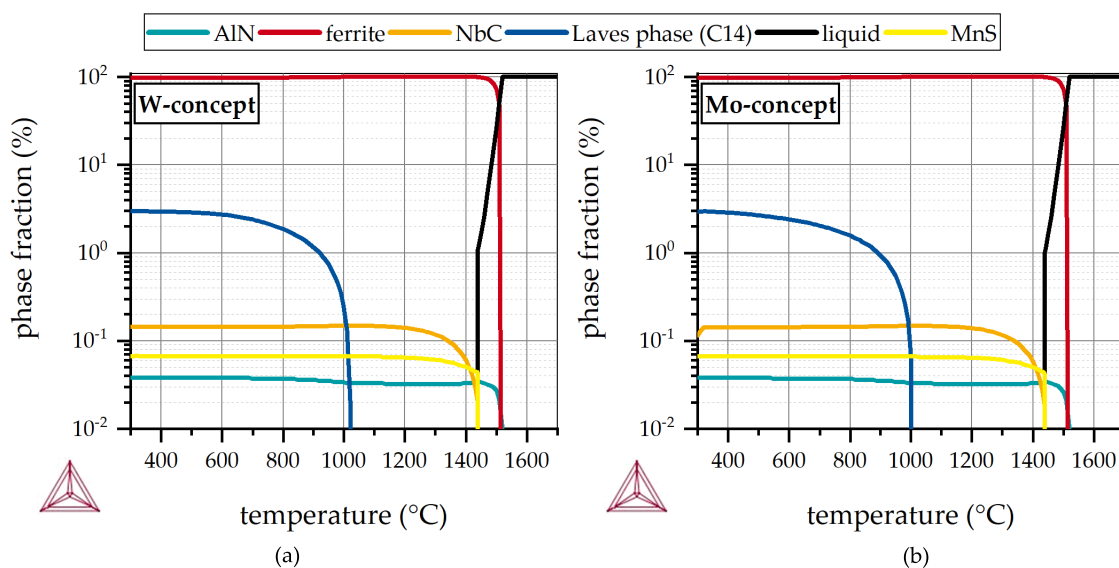


**Figure 2.** Results of the thermodynamic simulations for W- (a) and Mo-concept (b) using THERMOCALC with database TCFE9.

In a combined analysis of BSE images and EDS measurements (Figure 3, Table 2), precipitations no. 1, 6, and 8 mostly contain Nb and C. These precipitates are most likely the predicted NbC. Precipitations no. 2 and 5 contain mostly Al and N. These precipitates are most likely AlN. Both types of precipitations are also calculated by thermodynamic simulations (Figure 2). MnS could not be identified. After aging at 650 °C for 8 h (Figure 3b,e), new precipitates could be detected on the grain boundaries as well as inside the grain. The chemical composition of these phases is given in Table 2.

As shown in Table 2, precipitations no. 3, 4, 7 and 9 are enriched with Nb and Si in both concepts. Additionally, these precipitates contain W or Mo, respectively. In other studies [21,29,37] precipitates with very similar chemical composition are identified as C14 Laves phase with hexagonal crystal structure.

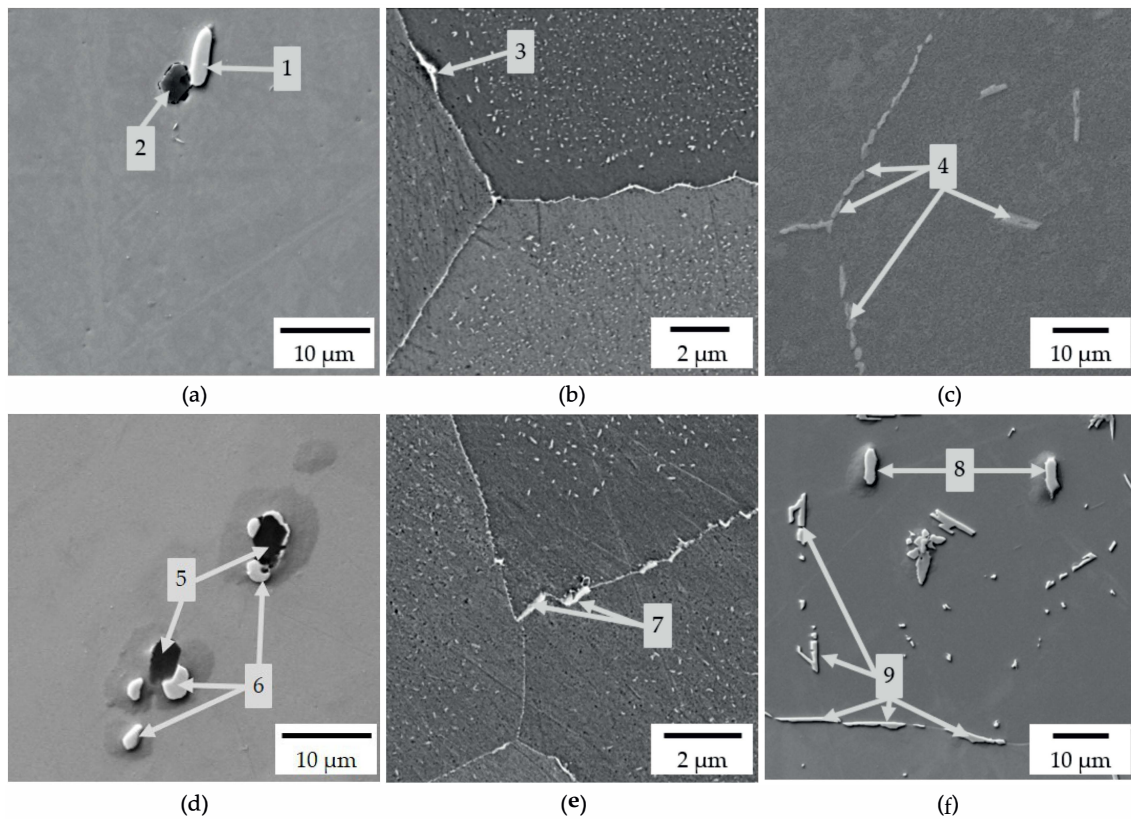


**Figure 3.** SEM images of the solution annealed state of the W-(a) and Mo-concept (d), as well as the 650 °C 8 h aged samples of W-(b) and Mo-concept (e) and 750 °C 8 h aged samples of W-(c) and Mo-concept (f).

**Table 2.** Chemical composition (wt. %) of precipitates displayed in Figure 3 measured by EDS.

Alloy	State	Precipitation No.	Fe	Al	Si	Nb	W	Mo	C	N
W-concept	solution annealed	1	4.5	—	—	75.3	—	—	17.6	1.6
		2	5.2	62.4	—	—	—	—	3.0	28.3
	650 °C 8 h	3	59.0	—	2.1	27.4	6.5	—	2.4	—
	750 °C 8 h	4	55.4	—	3.1	31.6	0.4	—	1.9	—
Mo-concept	solution annealed	5	2.5	65.0	—	—	—	—	2.7	27.3
		6	3.4	—	—	77.0	—	—	17.1	1.0
	650 °C 8 h	7	55.7	—	4.7	29.9	—	3.9	3.6	—
	750 °C 8 h	8	3.6	—	—	77.4	—	—	17.2	1.1
		9	51.1	—	4.5	34.3	—	4.1	3.1	—

### 3.2. X-ray Diffraction Analysis

The results of the XRD analysis are shown in Figure 4. For a clear arrangement, the intensity on the y-axis is displayed in logarithmic representation. The measurements were performed in the  $2\theta$  range from 30° to 110°; however, no peaks could be detected between  $2\theta$  angles of 30° to 40°. Among 60° and 110°, only two ferrite peaks could be detected in each steel. In the W-concept, the (002) ferrite peak is at 76.2°, and the (112) ferrite peak is at 98.7°. In the Mo-concept, the (002) ferrite peak is at 76.5°, and the (112) ferrite peak at 98.7°. No other peaks could be identified within the  $2\theta$  range of 60–110°. For this reason the x-axis shows a section of  $2\theta$  angles between 40° and 60°.

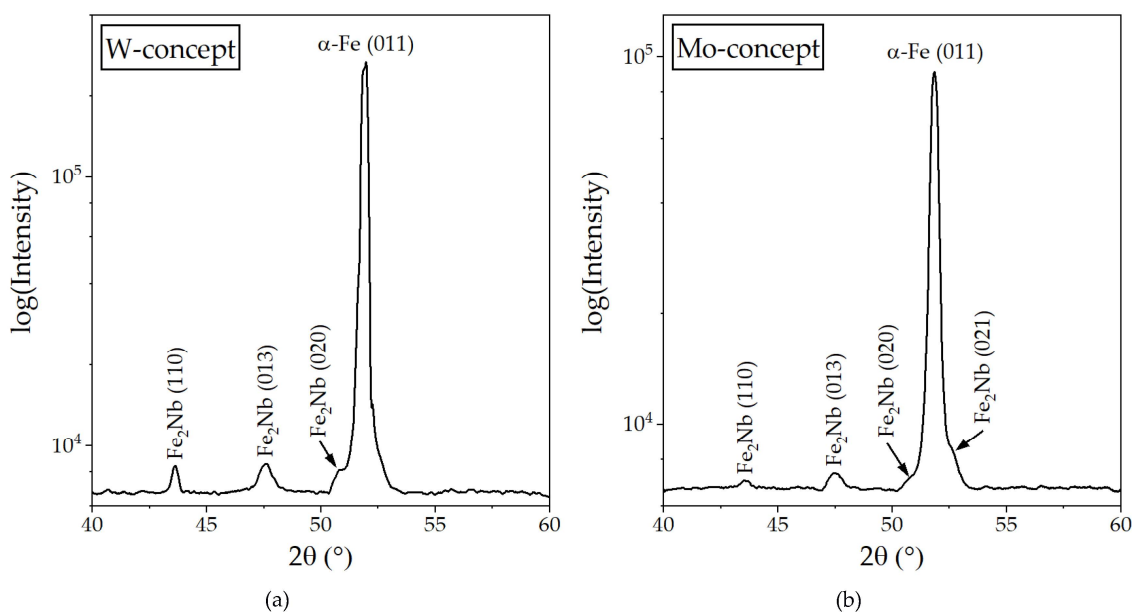


**Figure 4.** X-ray diffraction patterns of W-(a) and Mo-concept (b) both aged at 650 °C for 8 h.

The main peak in Figure 4a as well as in Figure 4b was identified at an  $2\theta$  angle of 51.9° (a) and 51.8° (b) as ferrite. The two peaks in Figure 4a at 43.6° and 47.6° are identified as  $\text{Fe}_2\text{Nb}$ . The peak at 50.8° slightly coincides with the ferrite peak. Nevertheless, indexing  $\text{Fe}_2\text{Nb}$  is possible. In Figure 4b, there are three  $\text{Fe}_2\text{Nb}$  peaks at 43.5°, 47.5°, and 50.8°. Compared to the W-concept (Figure 4a), another  $\text{Fe}_2\text{Nb}$  peak occurs at 52.6° in the Mo-concept. Both peaks at 50.8° and 52.6° coincide with the ferrite peak. However, the intensity of both peaks is high enough to indicate the  $\text{Fe}_2\text{Nb}$  phase.

It is obvious from Figure 4 that in both concepts the thermally induced precipitation is the  $\text{Fe}_2\text{Nb}$  phase which belongs to the group of C14 Laves phase. Figure 2 shows that there is a slight enrichment of W or Mo in the Laves phase, but it is too small for shifting the  $\text{Fe}_2\text{Nb}$  peaks. The thermally precipitated phase is therefore  $\text{Fe}_2\text{Nb}$  enriched with small amounts of W or Mo, respectively.

The formation of iron aluminides such as  $\text{FeAl}$  and  $\text{Fe}_3\text{Al}$  which were found in steels with Al contents above 20 at. % [38–40] did not occur. The Al content of the here-studied materials (approx. 11.5 at. %) is not high enough to form these structures.

The identification of  $\text{NbC}$  and  $\text{AlN}$  by XRD analysis for the studied alloying concepts is not possible. In both alloying concepts, the calculated phase fractions of  $\text{NbC}$  and  $\text{AlN}$  (Figure 2) are  $10^2$  times lower than the fraction of Laves phase. It can be assumed that the volume fraction of both phases is not high enough to identify them by XRD analysis.

### 3.3. Influence of Aging Temperature and Time on Hardness

In order to estimate the influence of the intermetallic Laves phase on the strength of the alloys, hardness measurements were carried out. The hardness profile as a function of aging time for different temperatures can be seen in Figure 5. In the solution-annealed state, the hardness for both concepts is between 215 and 220 HV10. In this state, the hardness is mainly attributed to solid solution hardening as a result of alloying with Nb, W, Mo, Al, Si, and Mn. The impact of these elements on solid solution hardening was also reported by other studies [41–44].

The increase in hardness with continued aging time is caused by the precipitation of the intermetallic Laves phase, whereby the matrix is first depleted of Nb [45,46] and, during the continued aging, also depleted of W [23] or Mo [30]. While Al, Mn, and Si remain in the matrix and thus form the basic contribution to solid solution hardness, the weight fraction of Nb decreases in both concepts with increasing holding time, whereby the solid solution hardening is reduced [41,47]. When Mo or W is incorporated into the Laves

phase during further progress of aging, the contribution of the solid solution hardening decreases further [42,48–51].

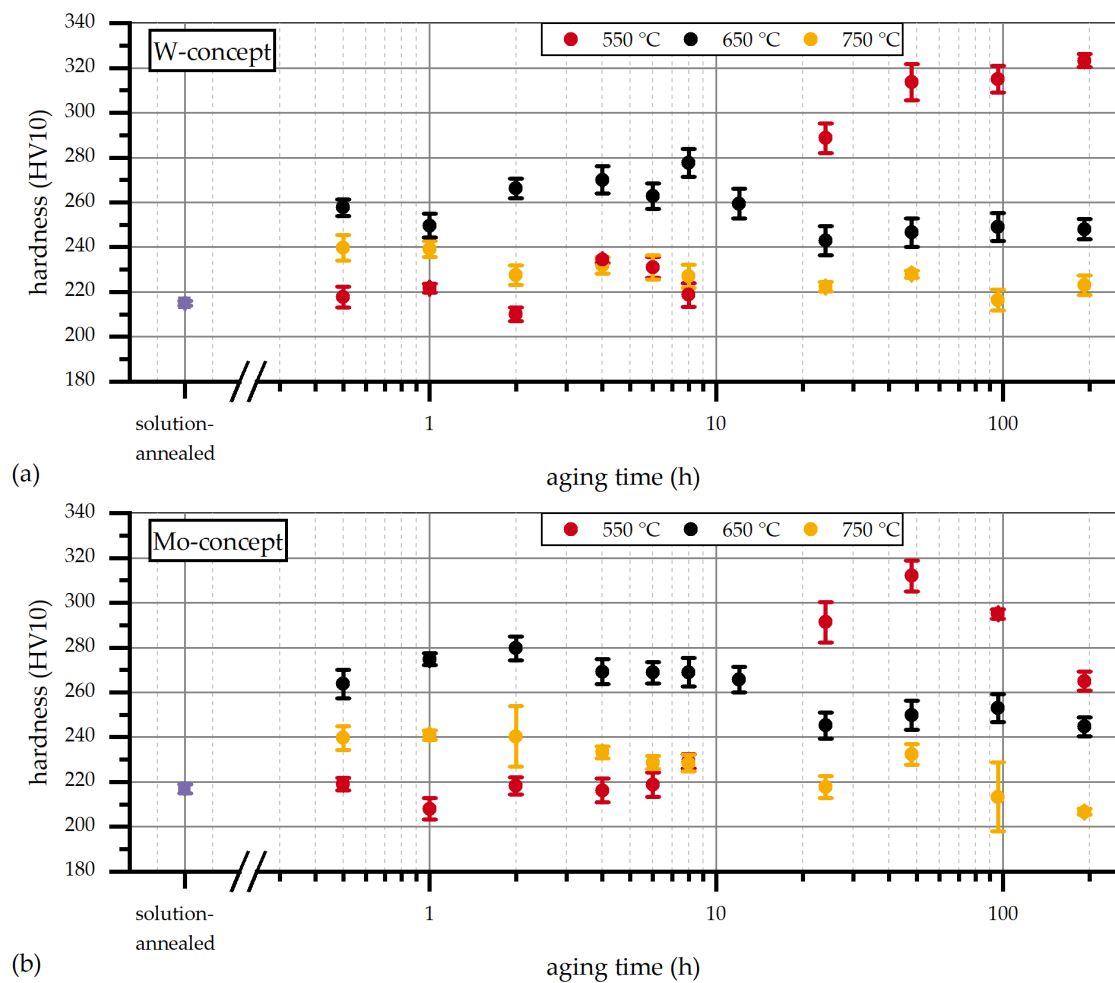


**Figure 5.** (a,b) Hardness vs. aging time at 550, 650, and 750 °C for both alloying concepts.

The composition of the matrix as a function of aging time can be taken from Table 3. It is demonstrated that with the increasing holding time, the matrix is depleted of Nb and W in the W-concept and of Nb and Mo in the Mo-concept. While Mo was removed from the matrix already after 4 h, the depletion of W in the matrix occurred only after 12 h.

**Table 3.** Matrix composition (wt. %) in dependency of the aging time at 650 °C for both alloying concepts measured by EDS.

Alloy	Aging Temperature	Aging Time	Fe	Al	Si	Mn	Nb	W	Mo
W-concept	650 °C	1 h	91.0	5.5	0.5	0.3	1.1	1.3	–
		4 h	90.7	5.9	0.5	0.3	0.7	1.3	–
		12 h	86.7	11.1	0.9	0.3	0.7	0.4	–
	750 °C	8 h	92.1	5.5	0.4	0.3	0.1	1.0	–
Mo-concept	650 °C	1 h	91.7	6.0	0.5	0.3	0.8	–	0.7
		4 h	92.4	5.8	0.5	0.3	0.6	–	0.5
		12 h	92.8	5.5	0.4	0.3	0.5	–	0.5
	750 °C	8 h	92.7	6.0	0.4	0.3	–	–	0.4

### 3.3.1. Early Stages of Aging at 650 °C

The aging temperature of 650 °C is of particular interest, since a substantial increase in hardness can be achieved after a significantly shorter holding time compared to aging at 550 °C. Rapid aging is particularly important for applications in the powertrain of motor vehicles, as shorter aging times can save energy and reduce production costs.

For both alloys, the considerable increase in hardness (40 HV10) occurs in the first 30 min of heat treatment at 650 °C, while with longer holding times, the hardness can only be increased by 20 HV10 (Figure 5). This suggests that nucleation and growth of the strength-increasing phase already take place in the first half hour of heat treatment, regardless of the alloying concept.

In general, two nucleation sites were identified: the grain boundaries and the grain interior. Furthermore, precipitation-free zones (PFZ) were detected along the grain boundaries. These PFZs have already been found in ferritic steels with Cr contents above 17 wt. % and the addition of Nb and W or Nb and Mo [20,52]. It can be assumed that the Laves phase-forming elements (Nb, W, Mo) diffuse to vacancies in the lattice due to their atomic size and occupy energetically more favourable positions, which was also reported by Liu et al. [53] and Askeland and Wright [54]. This leads to the formation of elongated precipitates of the composition Fe<sub>2</sub>Nb along the grain boundaries, which can be enriched with W and Mo, respectively.

Significantly finer particles can be found in the interior of the grains. According to Liu et al. [53], the formation of these particles can only take place when the nucleation sites along the grain boundaries are almost completely occupied. The formation of the Laves phase on the grain boundaries is much faster than in the inner grains. This behaviour was also shown by Sello and Stumpf [7] and by Kuhn et al. [20].

Due to the performed solution annealing prior to aging, it can be assumed that nearly no dislocations are available as potential nucleation sites in the inner grains. The formation of the Laves phase in the grain interior is based on the formation of clusters of Laves phase-forming elements. According to Hornebogen [55], these clusters form as follows. As a result of the temperature effect, vacancy rings, whose number increases with increasing holding time, form in the {100} plane of ferrite. Amara et al. [56] state that in Fe-Al alloys, the vacancies can be introduced into the material by quenching from high temperatures. Elements such as Mo accumulate in the stress fields of these quenched-in vacancy rings, leading to the formation of Mo clusters. If a local concentration of 33 at. % is exceeded as a result of the enrichment of Mo, the Fe<sub>2</sub>Mo phase forms, which was reported by Fernandez Guillermet [57]. The theory of clustering is often applied in the literature [58–61] as a precursor to precipitation formation. In a further study [61,62], the clustering of Nb was demonstrated analogously to the clustering of Mo. In order to be able to prove the clustering of the elements in the alloys investigated in the present study, it would be advisable to carry out detailed investigations by atom probe tomography (APT) after short holding times (less than 30 min).

### 3.3.2. Evolution of Laves Phase at 650 °C

It is interesting to note that in the Mo-concept a hardness of 280 HV10 is achieved after only 2 h, whereas in the W-concept a hardness of 280 HV10 is only reached after 8 h. In a different study [63], it was already shown that the precipitation of the Fe<sub>2</sub>Nb phase is accelerated by the addition of Mo. While in the Mo-concept Laves phase can already be found inside the grains after 2 h, in the W-concept, the Laves phase is mainly found along grain boundaries. Precipitation in the grain interior has not yet taken place. Complete precipitation in the grain interior can be found after 4 h in the W-concept. Comparing the diffusion coefficients of alloying elements in  $\alpha$ -Fe, Mo has a higher diffusion coefficient at 650 °C ( $D_{\text{Mo in } \alpha} = 3.46 \times 10^{-19} \text{ m}^2/\text{s}$ ) than W ( $D_{\text{W in } \alpha} = 2.19 \times 10^{-19} \text{ m}^2/\text{s}$ ) [64,65]. In the Mo-concept, the incorporation of Mo into the Laves phase can therefore proceed faster than the incorporation of W in the W-concept, which is why the growth of the Laves phase proceeds faster in the Mo-concept. Dong et al. [10] reported that the coarsening

of the Laves phase in connection with W proceeds more slowly than with Mo. This is also supported by Figure 6. While in the Mo-concept, the frequency of particles with an ECD of 20–40 nm tends to decrease with increasing holding time and the frequency of particles in the 60–80 nm class range increases, and no significant change can be found in the W-concept.

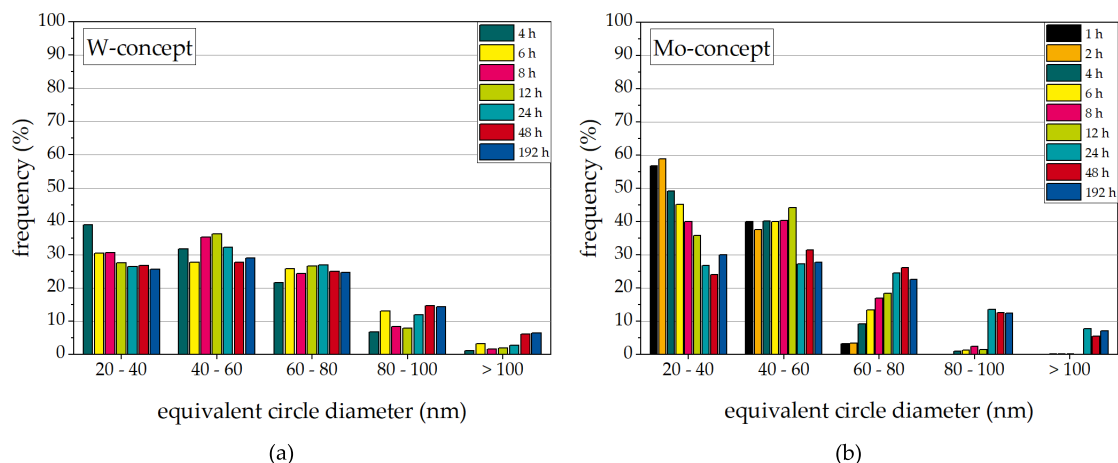


**Figure 6.** ECD of W- (a) and Mo-concept (b) as function of aging time at 650 °C.

Elsewhere in the literature [53,66], it was stated that alloying with W lowers the diffusion coefficient of dissolved atoms, which delays the coarsening process. The matrix in the Mo-concept is depleted in Nb and Mo with increasing holding time, while the matrix in the W-concept is exclusively depleted in Nb, which is shown by the results of EDS measurements (Table 3). Mo is thus incorporated faster into the Laves phase, while W remains longer in the matrix. Nevertheless, it can be deduced from Table 2 that W is incorporated into the Laves phase with longer aging time. Due to the high diffusion coefficient of Nb, compared to W and Mo [64,65,67], the phase  $\text{Fe}_2\text{Nb}$  forms first, which then becomes  $\text{Fe}_2(\text{Nb},\text{W})$  or rather  $\text{Fe}_2(\text{Nb},\text{Mo})$  which is comparable to the results of Miyazaki et al. [68].

Another indicator for the faster coarsening in the Mo-concept was derived from the area fraction of Laves phase in the inner grains (Figure 7a). While in the Mo-concept the maximum proportion of the Laves phase is already precipitated after 2 h, this is only the case after 8 h in the W-concept. Liu et al. [53] stated that complete precipitation of the phase is a necessary prerequisite for coarsening by Ostwald ripening mechanism. The driving force of the coarsening is associated with the coherence stresses between the bcc matrix and the hcp Laves phase. The stress fields around the Laves phase are energetically favourable sites for elements such as Nb, W, and Mo. The diffusion of these elements into the Laves phase causes coarsening. This phenomenon was already described by Sim et al. [46] and Ghosh [69].

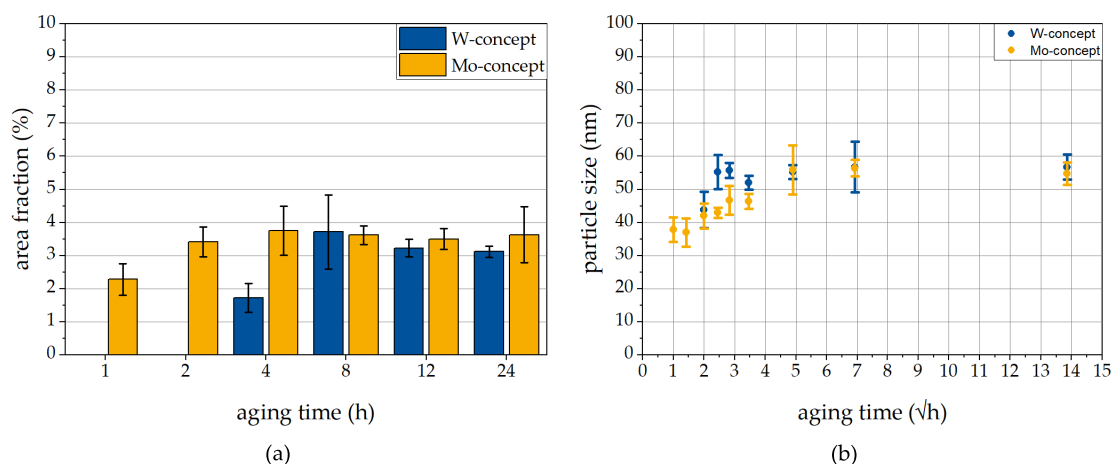


**Figure 7.** Area fraction of Laves phase in dependency of aging time (a) and particle size as function of the square root aging time (b) both aged at 650 °C for W- and Mo-concept.

### 3.3.3. Hardness Profile for Aging at 550 °C

The hardness of both alloys at 550 °C does not undergo any significant change within the first 8 h of heat treatment compared to the initial state. This is related to the incubation time of nucleation. Due to the low temperature, the element transport of Nb by diffusion (see [67]) is very slow compared to higher temperatures. According to Section 3.3.1, the preliminary stage of nucleation is the enrichment of Nb at vacancies. In reference to Alam et al. [61] and Pereloma et al. [62], this step is diffusion controlled. Appropriately, the time-consuming step is the enrichment of atoms at vacancies. As stated by Gottstein [70], the diffusion path ( $X$ ) which can be covered by an atom during a specific time ( $t$ ) at a given temperature is expressed as follows:

$$X^2 = 6 \cdot Dt \quad (1)$$

where  $D$  is the temperature-dependent diffusion coefficient. Since the initial state of all samples in this research series is the same, the diffusion path ( $X$ ) for this consideration is always the same. Therefore, Equation (1) can be transformed:

$$t_{550^\circ\text{C}} = \frac{D_{650^\circ\text{C}}}{D_{550^\circ\text{C}}} \cdot t_{650^\circ\text{C}} \quad (2)$$

Using the diffusion coefficients of Nb in  $\alpha$ -iron at 550 °C ( $D_{550^\circ\text{C}} = 3.37 \times 10^{-21} \text{ m}^2/\text{s}$ ) and 650 °C ( $D_{650^\circ\text{C}} = 5.04 \times 10^{-19} \text{ m}^2/\text{s}$ ) reported by Oono et al. [67] in Equation (2), the following relationship is obtained:

$$t_{550^\circ\text{C}} = 150 \cdot t_{650^\circ\text{C}} \quad (3)$$

This explains why an increase in hardness after aging at 550 °C can only be detected after significantly longer holding times compared to aging at 650 °C. Unfortunately, the incubation time cannot be determined from the experimental data so far. To obtain the experimental incubation time for both materials, in-situ synchrotron X-ray diffraction experiments at different aging temperatures need to be performed.

The hardness in both concepts increases between 8 and 48 h to approx. 320 HV10. While in the Mo-concept, the hardness drops after 48 h and reaches approx. 260 HV10 after 192 h, the hardness in the W-concept remains constant at 320 HV10. It can be assumed that due to the already discussed differences in the diffusion coefficients [64,65,67] a faster coarsening occurs in the Mo-concept and therefore the hardness decreases. However, this must be clarified by smaller temperature steps and high-resolution materials characterisation.

### 3.3.4. Hardness Profile for Aging at 750 °C

During aging at 750 °C, no significant increase in hardness can be achieved in none of the two alloying concepts. Compared to 550 and 650 °C the hardness can only be increased by 20 HV10 versus the initial state due to faster coarsening at 750 °C. The incubation time of the nucleation of the Laves phase is well below 30 min. Hu et al. [71] were able to show that the incubation time decreases with increasing temperature and that nuclei capable of growth are rapidly formed. Due to the influence of temperature, the formed precipitates grow rapidly and remove solid solution hardening elements (Nb, W, Mo) from the matrix, which was also reported by Nabiran et al. [45,72]. As claimed by Tokizane et al. [73] and Nabiran et al. [45], Laves phase coarsening by Ostwald ripening takes place afterwards. The decrease in hardness-increasing elements was detected by EDS (Table 3), which leads in combination with the Laves phase coarsening to a drop in hardness, which is in good comparison to the results of Juuti et al. [74] and Guo et al. [75].

The accelerated coarsening of Laves phase at higher temperatures was also reported by Kuhn et al. [21] as well as Sello and Stumpf [7] in high Cr-alloyed steels.

### 3.4. Influence of Laves Phase on Tensile Properties

At room temperature, all tensile specimens fail during homogeneous work hardening, i.e., before necking of the samples sets in. Therefore, only the influence of the Laves phase on the yield strength is considered in the following section.

Analysing the yield strength at room temperature, it can be seen from Figure 8 that the yield strength in the solution-annealed state for both alloying concepts is comparable. Since no Laves phase is precipitated in this state and the grain size in both concepts is above 350 µm, it can be assumed that the strength is caused by solid solution strengthening mainly [41,47,76]. According to Li [48] and Lacy and Gensamer [77], W and Mo have a comparable influence on solid solution strengthening at room temperature.

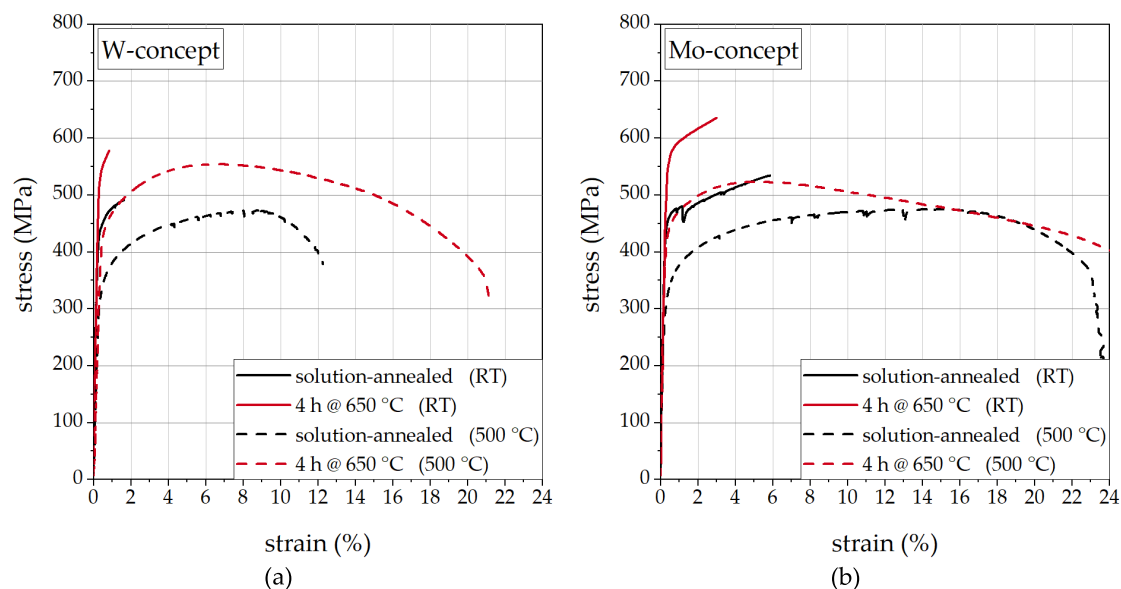


**Figure 8.** Stress–strain curves recorded at room temperature and at 500 °C of tensile samples of W-(a) and Mo-concept (b) in solution annealed state as well as aged at 650 °C for 4 h.

When aged at 650 °C for 4 h, the yield strength increases by 101 MPa in the W-concept and by 107 MPa in the Mo-concept. Considering Figure 7b, it can be seen that the particle size is almost the same with  $42 \pm 4$  and  $44 \pm 5$  nm for the Mo-concept and W-concept, respectively. Thus, the influence of the precipitate size on the yield strength can be neglected. Figure 7a shows that after aging at 650 °C for 4 h the area fraction of Laves phase in the W-concept is lower ( $1.7 \pm 0.4\%$ ) than in Mo-concept ( $3.7 \pm 0.7\%$ ). Considering Table 3, the

Nb content of the W-concept is higher, and no depletion of W took place after aging, which indicates that the lower proportion of precipitation hardening is compensated by solid solution strengthening by W.

Evaluating the stress–strain curves at a testing temperature of 500 °C (Figure 8), the stress difference of the yield strength in the solution-annealed state and in the aged state is 100 MPa in the W-concept and 104 MPa in the Mo-concept. Comparing these results to room temperature testing, it can be concluded that the precipitation hardening does not lose its effect at 500 °C. Comparing the results of solid solution strengthening effect of W at room temperature reported by Lacy and Gensamer [77] with its effect at 700 °C [49], W proves itself to be an extremely effective element for solid solution strengthening. Therefore, it can be supposed that the solid solution strengthening effect of W at 500 °C still compensates the lower phase fraction of the Laves phase in the W-concept. The fracture surfaces of tensile samples of different states of W- and Mo-concept can be seen in Figure 9. In the Mo-concept, the fracture behaviour changes from transgranular in the solution annealed state to intergranular in the aged state. The change in fracture behaviour is due to the weakening of the grain boundaries by precipitation of the Laves phase, which was also observed in previous studies [15,78,79].

Figure 9e shows small precipitates on the fracture surface of Mo-concept aged at 650 °C for 4 h. The chemical composition of these particles can be seen in Table 4. Comparing the measurement results from Tables 2 and 4 and additionally considering the discussion in Section 3.2, the precipitations on the fracture surface were identified as Laves phase. Therefore, the toughening of the material would require a grain refinement. Respective investigations, applying thermomechanical treatment aiming at dynamic recrystallization, are subject of ongoing work.

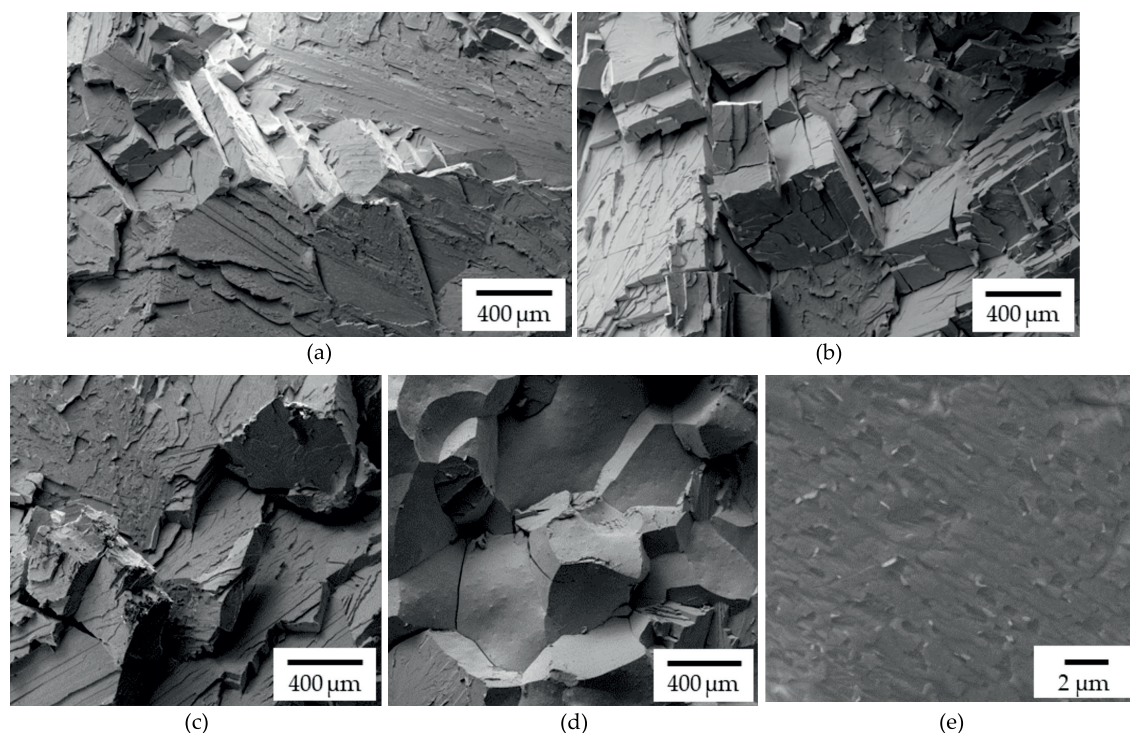


**Figure 9.** Tensile sample fracture surface of W-concept in solution annealed state (a) and aged at 650 °C for 4 h (b) as well as fracture surface of Mo-concept in solution annealed state (c) and aged at 650 °C for 4 h (d,e).

In contrast to the Mo-concept, the W-concept shows transgranular fracture in both states, solution-annealed and aged, respectively. Considering that precipitation of Laves phase at 650 °C is not completely finished after 4 h the diminish impact of this phase on grain boundaries is too low for a change in fracture mode.

**Table 4.** Chemical composition (wt. %) analyzed by EDS at different measuring sites of the fracture surfaces shown in Figure 9.

Alloy	State	Measuring Site	Fe	Al	Si	Mn	Nb	W	Mo
W-concept	solution annealed 4 h at 650 °C	fracture surface	90.0	5.5	0.5	0.3	1.0	1.3	–
		fracture surface	90.4	5.6	0.4	0.3	1.0	1.3	–
Mo-concept	solution annealed 4 h at 650 °C 4 h at 650 °C	fracture surface	89.8	6.3	0.6	0.3	1.2	–	0.7
		fracture surface	87.1	2.0	1.3	0.4	8.5	–	–
		precipitation	79.9	–	2.1	–	13.2	–	1.5

#### 4. Conclusions

The CALPHAD-guided development of a new low-density, high-strength forging steel for automotive power train applications led to two promising Laves phase strengthening W/Mo alloying concepts: Fe-6 wt. % Al-0.25 wt. % Mn-1.25 wt. % Nb-0.5 wt. % Si plus 1.25 wt. % W or 0.75 wt. % Mo, respectively. According to the results of the materials characterisation the following conclusions were drawn:

1. Aging at temperatures between 550 and 750 °C leads in the investigated W- and Mo-alloyed steels to the formation of the intermetallic Fe<sub>2</sub>Nb Laves phase. Aside from Fe and Nb, small amounts of W or Mo as well as Si were found to be incorporated in the Laves phase.
2. The most powerful effect of precipitation hardening occurs in both alloying concepts at 550 °C. At 650 °C, the increase in hardness is less pronounced but occurs after a significantly shorter aging time due to the higher diffusion coefficients of Nb, W, and Mo at 650 °C compared to 550 °C. Aging at 750 °C leads to no significant increase in hardness for both alloying concept since the formation and coarsening of the Laves phase is very fast at this temperature.
3. At 550 °C, the precipitation hardening in the Mo-concept is less stable than in the W-concept which might be contributed to the higher diffusion coefficient of Mo and the accelerated diffusion of Nb in presence of Mo. Further investigations have to be performed to clarify the effect of W and Mo on coarsening of the Laves phase at 550 °C.
4. The yield strength can be substantially increased by precipitation hardening with the intermetallic Laves phase. The effect of precipitation hardening is still present and not lowered at testing temperatures of 500 °C in comparison to the effect of precipitation hardening at room temperature.

**Author Contributions:** Conceptualization, R.E.; methodology, R.E.; validation, R.E. and U.K.; formal analysis, R.E.; investigation, R.E.; data curation, R.E.; writing—original draft preparation, R.E.; writing—review and editing, R.E. and U.K.; visualization, R.E.; supervision, U.K.; project administration, R.E. and U.K.; funding acquisition, U.K. All authors have read and agreed to the published version of the manuscript.

**Funding:** The project on which this report is based was funded by the Federal Ministry of Education and Research of the Federal Republic of Germany under the funding code 03XP0172D. The responsibility for the content of this publication lies with the author.

**Institutional Review Board Statement:** Not applicable.

**Informed Consent Statement:** Not applicable.

**Data Availability Statement:** The data presented in this study are available on request from the corresponding author.

**Acknowledgments:** The authors gratefully acknowledge the support of H. Breitbach, C. Freytag, R. Gier, W. Tupiec, M. Schillheim, J. Dartenne, S. Vinke, N. Boinski, and M. Dorenwendt in dilatometry

experiments, metallography, and mechanical testing. Special thanks are contributed to C. Blankart, J. Pöpperlová, and A. Gramlich for reviewing and fruitful discussions. Additionally, we would like to thank D. Zander and M. Thönnißen from the Foundry Institute of the RWTH Aachen University for the quick handling of the XRD measurements.

**Conflicts of Interest:** The authors declare no conflict of interest.

## References

1. MAHLE GmbH. (Ed. *Kolben und Motorische Erprobung*, 1st ed.; ATZ/MTZ-Fachbuch, Vieweg+Teubner: Wiesbaden, Germany, 2011. [[CrossRef](#)]
2. Krüger, L.; Jentsch, E.; Brunke, L.; Keßler, A.; Wolf, G.; Lehnert, T.; Schubert, N.; Wagner, A.; Landgrebe, D. Development of an innovative lightweight piston through process combination “casting–forging”. *Procedia Manuf.* **2019**, *27*, 172–176. [[CrossRef](#)]
3. Niu, D.; Zhang, J.; Xiong, P.; Hao, G.; Liu, S.; Guo, W. High temperature fatigue and oxidation characteristics of forged steel piston materials. *Eng. Fail. Anal.* **2019**, *97*, 220–226. [[CrossRef](#)]
4. Zander, D.; Klink, A.; Harst, S.; Klocke, F.; Altenbach, C. Influence of machining processes on rim zone properties and high temperature oxidation behavior of 42CrMo4. *Mater. Corros.* **2019**, *70*, 2190–2204. [[CrossRef](#)]
5. Heizmann, J.; Blau, D. High-Strength Pistons for Diesel Engines. *Atzoffhighway Worldw.* **2018**, *11*, 40–43. [[CrossRef](#)]
6. Saxena, S.; Ambikesh, R.K. Design and finite element analysis of connecting rod of different materials. In *AIP Conference Proceedings*; AIP Publishing LLC: Melville, NY, USA, 2021; Volume 2341.
7. Sello, M.P.; Stumpf, W.E. Laves phase precipitation and its transformation kinetics in the ferritic stainless steel type AISI 441. *Mater. Sci. Eng. A* **2011**, *528*, 1840–1847. [[CrossRef](#)]
8. Reuther, F.; Mosel, A.; Freytag, P.; Lambarri, J.; Degenkolb, L.; Werner, M.; Winter, S. Numerical and experimental investigations for hot metal gas forming of stainless steel X2CrTiNb18. *Procedia Manuf.* **2019**, *27*, 112–117. [[CrossRef](#)]
9. Viswanathan, R.; Bakker, W. Materials for Ultrasupercritical Coal Power Plants—Boiler Materials: Part 1. *J. Mater. Eng. Perform.* **2001**, *10*, 81–95. [[CrossRef](#)]
10. Dong, J.; Yu, H.; Yoo, D.H.; Huynh, Q.; Shin, K. Effects of additional elements on the evolution of second phases in 9–12% Cr steel and resulting mechanical properties. *Int. J. Mod. Phys. B* **2009**, *23*, 1141–1147. [[CrossRef](#)]
11. Hosoi, Y.; Wade, N.; Kunimitsu, S.; Urita, T. Precipitation behavior of laves phase and its effect on toughness of 9Cr-2Mo Ferritic-martensitic steel. *J. Nucl. Mater.* **1986**, *141–143*, 461–467.
12. Tomaszewicz, P.; Wallwork, G.R. Observations of nodule growth during the oxidation of pure binary iron-aluminum alloys. *Oxid. Met.* **1983**, *19*, 165–185. [[CrossRef](#)]
13. Palm, M. Concepts derived from phase diagram studies for the strengthening of Fe–Al-based alloys. *Intermetallics* **2005**, *13*, 1286–1295. [[CrossRef](#)]
14. Rana, R.; Liu, C.; Ray, R.K. Low-density low-carbon Fe–Al ferritic steels. *Scr. Mater.* **2013**, *68*, 354–359. [[CrossRef](#)]
15. Falat, L.; Schneider, A.; Sauthoff, G.; Frommeyer, G. Mechanical properties of Fe–Al–M–C (M=Ti, V, Nb, Ta) alloys with strengthening carbides and Laves phase. *Intermetallics* **2005**, *13*, 1256–1262. [[CrossRef](#)]
16. Morris, D.G.; Muñoz-Morris, M.A.; Requejo, L.M.; Baudin, C. Strengthening at high temperatures by precipitates in Fe–Al–Nb alloys. *Intermetallics* **2006**, *14*, 1204–1207. [[CrossRef](#)]
17. Morris, D.G.; Requejo, L.M.; Muñoz-Morris, M.A. Age hardening in some Fe–Al–Nb alloys. *Scr. Mater.* **2006**, *54*, 393–397. [[CrossRef](#)]
18. Morris, D.G.; Requejo, L.M.; Muñoz-Morris, M.A. A study of precipitation in DO3 ordered Fe–Al–Nb alloy. *Intermetallics* **2005**, *13*, 862–871. [[CrossRef](#)]
19. Stein, F.; Schneider, A.; Frommeyer, G. Flow stress anomaly and order–disorder transitions in Fe<sub>3</sub>Al-based Fe–Al–Ti–X alloys with X=V, Cr, Nb, or Mo. *Intermetallics* **2003**, *11*, 71–82. [[CrossRef](#)]
20. Kuhn, B.; Jimenez, C.A.; Niewolak, L.; Hüttl, T.; Beck, T.; Hattendorf, H.; Singheiser, L.; Quadackers, W.J. Effect of Laves phase strengthening on the mechanical properties of high Cr ferritic steels for solid oxide fuel cell interconnect application. *Mater. Sci. Eng. A* **2011**, *528*, 5888–5899. [[CrossRef](#)]
21. Kuhn, B.; Talik, M.; Niewolak, L.; Zurek, J.; Hattendorf, H.; Ennis, P.J.; Quadackers, W.J.; Beck, T.; Singheiser, L. Development of high chromium ferritic steels strengthened by intermetallic phases. *Mater. Sci. Eng. A* **2014**, *594*, 372–380. [[CrossRef](#)]
22. Talik, M. Influence of Initial Thermomechanical Treatment on High Temperature Properties of Laves Phase Strengthened Ferritic Steels. Ph.D. Thesis, RWTH Aachen University-FZ Jülich, Aachen, Germany, 2016.
23. Pöpperlová, J.; Fan, X.; Kuhn, B.; Bleck, W.; Krupp, U. Impact of Tungsten on Thermomechanically Induced Precipitation of Laves Phase in High Performance Ferritic (HiperFer) Stainless Steels. *Appl. Sci.* **2020**, *10*, 4472. [[CrossRef](#)]
24. Chai, Y.W.; Kato, K.; Yabu, C.; Ishikawa, S.; Kimura, Y. Disconnections and Laves (C14) precipitation in high-Cr ferritic stainless steels. *Acta Mater.* **2020**, *198*, 230–241. [[CrossRef](#)]
25. Fan, X.; Kuhn, B.; Pöpperlová, J.; Bleck, W.; Krupp, U. Compositional Optimization of High-Performance Ferritic (HiperFer) Steels—Effect of Niobium and Tungsten Content. *Metals* **2020**, *10*, 1300. [[CrossRef](#)]
26. Stein, F.; Palm, M.; Sauthoff, G. Structure and stability of Laves phases. Part I. Critical assessment of factors controlling Laves phase stability. *Intermetallics* **2004**, *12*, 713–720. [[CrossRef](#)]

27. Maier, H.J.; Niendorf, T.; Bürgel, R. *Handbuch Hochtemperatur-Werkstofftechnik: Grundlagen, Werkstoffbeanspruchungen, Hochtemperaturlegierungen und -Beschichtungen*, 5th ed.; Springer Fachmedien Wiesbaden: Wiesbaden, Germany, 2015. [CrossRef]
28. Aghajani, A.; Richter, F.; Somsen, C.; Fries, S.G.; Steinbach, I.; Eggeler, G. On the formation and growth of Mo-rich Laves phase particles during long-term creep of a 12% chromium tempered martensite ferritic steel. *Scr. Mater.* **2009**, *61*, 1068–1071. [CrossRef]
29. Isik, M.I.; Kostka, A.; Eggeler, G. On the nucleation of Laves phase particles during high-temperature exposure and creep of tempered martensite ferritic steels. *Acta Mater.* **2014**, *81*, 230–240. [CrossRef]
30. Xia, Z.X.; Wang, C.Y.; Zhao, Y.F.; Zhang, G.D.; Zhang, L.; Meng, X.M. Laves Phase Formation and Its Effect on Mechanical Properties in P91 Steel. *Acta Metall. Sin.* **2015**, *28*, 1238–1246. [CrossRef]
31.  $\alpha$ -Fe (ferrite) (Fe<sub>rt</sub>) Crystal Structure: Datasheet from “PAULING FILE Multinaries Edition-2012” in SpringerMaterials. Available online: [https://materials.springer.com/isp/crystallographic/docs/sd/\\_1817302](https://materials.springer.com/isp/crystallographic/docs/sd/_1817302) (accessed on 11 October 2021).
32. Fe<sub>2</sub>Nb (NbFe<sub>2</sub>) Crystal Structure: Datasheet from “PAULING FILE Multinaries Edition-2012” in SpringerMaterials. Available online: [https://materials.springer.com/isp/crystallographic/docs/sd/\\_1011276](https://materials.springer.com/isp/crystallographic/docs/sd/_1011276) (accessed on 11 October 2021).
33. AlN Crystal Structure: Datasheet from “PAULING FILE Multinaries Edition-2012” in SpringerMaterials. Available online: [https://materials.springer.com/isp/crystallographic/docs/sd/\\_0533024](https://materials.springer.com/isp/crystallographic/docs/sd/_0533024) (accessed on 11 October 2021).
34. CNb (NbC) Crystal Structure: Datasheet from “PAULING FILE Multinaries Edition-2012” in SpringerMaterials. Available online: [https://materials.springer.com/isp/crystallographic/docs/sd/\\_0450232](https://materials.springer.com/isp/crystallographic/docs/sd/_0450232) (accessed on 11 October 2021).
35. Fe<sub>3</sub>Al Crystal Structure: Datasheet from “PAULING FILE Multinaries Edition-2012” in SpringerMaterials. Available online: [https://materials.springer.com/isp/crystallographic/docs/sd/\\_0452482](https://materials.springer.com/isp/crystallographic/docs/sd/_0452482) (accessed on 11 October 2021).
36. FeAl Crystal Structure: Datasheet from “PAULING FILE Multinaries Edition-2012” in SpringerMaterials. Available online: [https://materials.springer.com/isp/crystallographic/docs/sd/\\_0312257](https://materials.springer.com/isp/crystallographic/docs/sd/_0312257) (accessed on 11 October 2021).
37. Risanti, D.D.; Sauthoff, G. Microstructures and mechanical properties of Fe–Al–Ta alloys with strengthening Laves phase. *Intermetallics* **2011**, *19*, 1727–1736. [CrossRef]
38. Morris, D.G.; Morris, M.A. Strengthening at intermediate temperatures in iron aluminides. *Mater. Sci. Eng. A* **1997**, *239*–240. [CrossRef]
39. Palm, M.; Stein, F.; Dehm, G. Iron Aluminides. *Annu. Rev. Mater. Res.* **2019**, *49*, 297–326. [CrossRef]
40. Stoloff, N.S. Iron aluminides: Present status and future prospects. *Mater. Sci. Eng. A* **1998**, *258*, 1–14. [CrossRef]
41. Kostryzhev, A.G.; Marenych, O.O.; Killmore, C.R.; Pereloma, E.V. Strengthening Mechanisms in Thermomechanically Processed NbTi-Microalloyed Steel. *Metall. Mater. Trans. A* **2015**, *46A*, 3470–3480. [CrossRef]
42. Verein Deutscher Eisenhüttenleute. (Ed.) *Werkstoffkunde Stahl: Band 1: Grundlagen*, 4th ed.; Springer: Berlin/Heidelberg, Germany; New York, NY, USA; Tokyo, Japan, 1984.
43. Lechner, C.; Seume, J.; Eds. *Stationäre Gasturbinen*, 3rd ed.; VDI-Buch, Springer: Berlin/Heidelberg, Germany, 2019. [CrossRef]
44. Mintz, B.; Gunawardana, W.D.; Su, H. Al as solid solution hardener in steels. *Mater. Sci. Technol.* **2008**, *24*, 596–600. [CrossRef]
45. Nabiran, N.; Klein, S.; Weber, S.; Theisen, W. Evolution of the Laves Phase in Ferritic Heat-Resistant Steels During Long-term Annealing and its Influence on the High-Temperature Strength. *Metall. Mater. Trans. A* **2015**, *46A*, 102–114. [CrossRef]
46. Sim, G.M.; Ahn, J.C.; Hong, S.C.; Lee, K.J.; Lee, K.S. Effect of Nb precipitate coarsening on the high temperature strength in Nb containing ferritic stainless steels. *Mater. Sci. Eng. A* **2005**, *396*, 159–165. [CrossRef]
47. Gladman, T. *The Physical Metallurgy of Microalloyed Steels*; Institute of Materials: London, UK, 1997.
48. Li, Q. Precipitation of Fe<sub>2</sub>W Laves Phase and Modeling of Its Direct Influence on the Strength of a 12Cr-2W Steel. *Metall. Mater. Trans. A* **2006**, *37A*, 89–97. [CrossRef]
49. Narita, T.; Ukai, S.; Ohtsuka, S.; Inoue, M. Effect of tungsten addition on microstructure and high temperature strength of 9CrODS ferritic steel. *J. Nucl. Mater.* **2011**, *417*, 158–161. [CrossRef]
50. Majta, J.; Lenard, J.G.; Pietrzyk, M. A study of the effect of the thermomechanical history on the mechanical properties of a high niobium steel. *Mater. Sci. Eng. A* **1996**, *208*, 249–259. [CrossRef]
51. Bose, S.C.; Singh, K.; Ray, A.K.; Ghosh, R.N. Effect of thermal ageing on mechanical properties and microstructures of a standard G-X 12 CrMoVWNbN 1011 grade of cast steel for turbine casing. *Mater. Sci. Eng. A* **2008**, *476*, 257–266. [CrossRef]
52. Juuti, T.; Rovatti, L.; Mäkelä, A.; Karjalainen, L.P.; Porter, D. Influence of long heat treatments on the laves phase nucleation in a type 444 ferritic stainless steel. *J. Alloys Compd.* **2014**, *616*, 250–256. [CrossRef]
53. Liu, H.; Wei, L.; Ma, M.; Zheng, J.; Chen, L.; Misra, R.D.K. Laves phase precipitation behavior and high-temperature strength of W-containing ferritic stainless steels. *J. Mater. Res. Technol.* **2020**, *9*, 2127–2135. [CrossRef]
54. Askeland, D.R.; Wright, W.J. *Essentials of Materials Science and Engineering*, 4th ed.; Cengage Learning: Boston, MA, USA, 2019.
55. Hornbogen, E. Clustering in an Alpha Iron-Molybdenum Solid Solution. *J. Appl. Phys.* **1961**, *32*, 135–139. [CrossRef]
56. Amara, H.; Fu, C.C.; Soisson, F.; Maugis, P. Aluminum and vacancies in  $\alpha$ -iron: Dissolution, diffusion, and clustering. *Phys. Rev. B* **2010**, *81*, 1409. [CrossRef]
57. Fernandez Guillermet, A. The Fe-Mo (Iron-Molybdenum) System. *Bull. Alloy. Phase Diagrams* **1982**, *3*, 359–367. [CrossRef]
58. Marcus, H.L.; Fine, M.E.; Schwartz, L.H. Mössbauer-Effect Study of Solid-Solution and Precipitated Fe-Rich Fe-Mo Alloys. *J. Appl. Phys.* **1967**, *38*, 4750–4758. [CrossRef]
59. Ericsson, T.; Mourikis, S.; Cohen, J.B. Clustering in Fe-Mo Alloys. *J. Mater. Sci.* **1970**, *5*, 901–908. [CrossRef]
60. Ustinovshikov, Y.I. Precipitation in solids. *J. Mater. Sci.* **1992**, *27*, 3993–4002. [CrossRef]

61. Alam, T.; Chaturvedi, M.; Ringer, S.P.; Cairney, J.M. Precipitation and clustering in the early stages of ageing in Inconel 718. *Mater. Sci. Eng. A* **2010**, *527*, 7770–7774. [[CrossRef](#)]
62. Pereloma, E.V.; Timokhina, I.B.; Russel, K.F.; Miller, M.K. Characterization of clusters and ultrafine precipitates in Nb-containing C–Mn–Si steels. *Scr. Mater.* **2006**, *54*, 471–476. [[CrossRef](#)]
63. Fujita, N.; Kikuchi, M.; Ohmura, K. Expressions for Solubility Products of Fe<sub>3</sub>Nb<sub>3</sub>C carbide and Fe<sub>2</sub>Nb Laves Phase in Niobium Alloyed Ferritic Stainless Steels. *ISIJ Int.* **2003**, *43*, 1999–2006. [[CrossRef](#)]
64. Takemoto, S.; Nitta, H.; Iijima, Y.; Yamazaki, Y. Diffusion of tungsten in  $\alpha$ -iron. *Philos. Mag.* **2007**, *87*, 1619–1629. [[CrossRef](#)]
65. Nitta, H.; Yamamoto, T.; Kanno, R.; Takasawa, K.; Iida, T.; Yamazaki, Y.; Ogu, S.; Iijima, Y. Diffusion of molybdenum in  $\alpha$ -iron. *Acta Mater.* **2002**, *50*, 4117–4125. [[CrossRef](#)]
66. Jeon, S.H.; Kim, S.T.; Lee, I.S.; Kim, J.S.; Kim, K.T.; Park, Y.S. Effects of W substitution on the precipitation of secondary phases and the associated pitting corrosion in hyper duplex stainless steels. *J. Alloys Compd.* **2012**, *544*, 166–172. [[CrossRef](#)]
67. Oono, N.; Nitta, H.; Iijima, Y. Diffusion of niobium in  $\alpha$ -iron. *Mater. Trans.* **2003**, *44*, 2078–2083. [[CrossRef](#)]
68. Miyazaki, A.; Takao, K.; Furukimi, O. Effect of Nb on the Proof Strength of Ferritic Stainless Steels at Elevated Temperatures. *ISIJ Int.* **2002**, *42*, 916–920. [[CrossRef](#)]
69. Ghosh, S. Kinetic study on the coarsening behaviour of equilibrium phases in Nb alloyed ferritic stainless steels at 700 °C. *Mater. Chem. Phys.* **2010**, *124*, 13–16. [[CrossRef](#)]
70. Gottstein, G. *Materialwissenschaft und Werkstofftechnik*; Springer: Berlin/Heidelberg, Germany, 2014. [[CrossRef](#)]
71. Hu, P.; Yan, W.; Sha, W.; Wang, W.; Guo, Z.L.; Shan, Y.Y.; Yang, K. Study on Laves phase in an advanced heat-resistant steel. *Front. Mater. Sci. China* **2009**, *3*, 434–441. [[CrossRef](#)]
72. Nabiran, N.; Weber, S.; Theisen, W. Influence of Laves Phase Precipitation and Coarsening on High-Temperature Strength of Ferritic Stainless Steels. *Steel Res. Int.* **2012**, *83*, 758–765. [[CrossRef](#)]
73. Tokizane, M.; Okada, Y.; Tamura, I. The Growth of Fe<sub>2</sub>Ti-Laves Phase Precipitates in Fe-Ti Alloy during Aging\*. *Trans. ISIJ* **1972**, *12*, 276–282. [[CrossRef](#)]
74. Juuti, T.J.; Karjalainen, L.P.; Heikkinen, E.P. Precipitation of Si and its Influence on Mechanical Properties of Type 441 Stainless Steel. *Adv. Mater. Res.* **2011**, *409*, 690–695. [[CrossRef](#)]
75. Guo, X.; Jiang, Y.; Gong, J.; Weng, X. The influence of long-term thermal exposure on microstructural stabilization and mechanical properties in 9Cr-0.5Mo-1.8 W-VNb heat-resistant steel. *Mater. Sci. Eng. A* **2016**, *672*, 194–202. [[CrossRef](#)]
76. Hall, E.O. The Deformation and Ageing of Mild Steel: III Discussion of Results. *Proc. Phys. Soc. Sect. B* **1951**, *64*, 747. [[CrossRef](#)]
77. Lacy, C.E.; Gensamer, M. The tensile properties of alloyed ferrites. *Trans. Am. Soc. Met.* **1944**, *32*, 88–105.
78. Sarwat, S.G.; Basu, J. Understanding Laves phase precipitation induced embrittlement of modified 9Cr–1Mo steel. *SN Appl. Sci.* **2019**, *1*, 5164. [[CrossRef](#)]
79. Komazaki, S.I.; Kishi, S.; Shoji, T.; Chiba, H.; Suzuji, K. Thermal Aging Embrittlement of Tungsten-Alloyed 9%Cr Ferritic Steels and Electrochemical Evaluation. *Mater. Sci. Res. Int.* **2003**, *9*, 42–49.